

A Hybrid semi-Lagrangian Flow Mapping Approach for Vlasov Systems

Combining Iterative and Compositional Flow Maps

Philipp Krah^{*†‡} Zetao Lin^{*†} R.-Paul Wilhelm[§] Fabio Bacchini^{§¶}
 Jean-Christophe Nave[¶] Virginie Grandgirard[‡] Kai Schneider[†]

January 30, 2026

Abstract

We propose a hybrid semi-Lagrangian scheme for the Vlasov–Poisson equation that combines the Numerical Flow Iteration (NuFi) method with the Characteristic Mapping Method (CMM). Both approaches exploit the semi-group property of the underlying diffeomorphic flow, enabling the reconstruction of solutions through flow maps that trace characteristics back to their initial positions. NuFi builds this flow map iteratively, preserving symplectic structure and conserving invariants, but its computational cost scales quadratically with time. Its advantage lies in a compact, low-dimensional representation depending only on the electric field. In contrast, CMM achieves low computational costs when remapping by composing the global flow map from explicitly stored submaps. The proposed hybrid method merges these strengths: NuFi is employed for accurate and conservative local time stepping, while CMM efficiently propagates the solution through submap composition. This approach reduces storage requirements, maintains accuracy, and improves structural properties. Numerical experiments demonstrate the effectiveness of the scheme and highlight the trade-offs between memory usage and computational cost. We benchmark against a semi-Lagrangian predictor–corrector scheme used in modern gyrokinetic codes, evaluating accuracy, conservation properties.

Keywords: Characteristic Mapping, Numerical Flow Iteration, Vlasov–Poisson, Flow Map, semi-Lagrangian

1 Introduction

This work addresses the efficient numerical resolution of fine-scale structures in collisionless kinetic plasma systems, a long-standing challenge in Vlasov-based simulations. Such structures can emerge from various physical effects: phase mixing of small perturbations, as in Landau damping; resonant interactions between counter-streaming electron populations leading to the two-stream instability; and many others. Accurately capturing these multiscale features requires numerical representations that remain both memory-efficient and computationally affordable. To this end, we introduce a new approach that exploits the semigroup properties of the characteristic flow. By representing the solution through a composition of flowmaps, rather than through increasingly dense phase space grids, we achieve a more scalable resolution of fine-scale dynamics than with conventional methods.

In this work, we focus on the one-dimensional, one-velocity (1D+1V) Vlasov–Poisson (VP) system,

$$\partial_t f + v \partial_x f + E \partial_v f = 0, \quad (1)$$

^{*}First authors: philipp.krah@univ-amu.fr, zeato.lin@edu.univ-amu.fr

[†]Aix-Marseille Université, I2M, CNRS, UMR 7373, 3 place Victor Hugo, 13331 Marseille cedex 3, France.

[‡]IRFM - CEA Cadarache, 13108 Saint-Paul-lez-Durance, France

[§]Centre for mathematical Plasma Astrophysics, Department of Mathematics, KU Leuven, B-3001 Leuven, Belgium

[¶]Royal Belgian Institute for Space Aeronomy, Solar-Terrestrial Centre of Excellence, B-1180 Uccle, Belgium

[¶]McGill University, Department of Mathematics and Statistics, Montreal, Canada

where f denotes the particle distribution function and E is the electric field

$$-\Delta_x \varphi = \rho = 1 - \int_{\mathbb{R}} f \, dv, \quad (2)$$

$$E = -\nabla_x \varphi. \quad (3)$$

The numerical treatment of the Vlasov equation is particularly demanding: The distribution function is in general defined over a six-dimensional (in this work, two-dimensional) phase space, which gives rise to the curse of dimensionality and thus forces practical simulations to rely on reduced models or coarse discretizations. In addition, the nonlinear and collisionless character of the VP dynamics promotes the formation of fine-scale filamentary structures in phase space. These filaments are notoriously difficult to resolve accurately, yet they are essential for understanding the onset of kinetic instabilities and may play a significant role in plasma heating and dissipation processes [46, 62, 63].

State of the Art Plasma Simulations

The numerical solution of the Vlasov equation generally employs methods falling into one of three classes: Eulerian (discrete velocity), Semi-Lagrangian, or Lagrangian, as discussed e.g. in reviews by Filbet and Sonnendrücker [27] and Palmroth et al. [54]. The first two approaches are grid-based, meaning that the solution f is represented on a discretization of the phase-space. Eulerian discretizations compute the evolution of the distribution by evaluating its local temporal derivative at each grid node, thereby recasting the Vlasov equation as a large coupled system of ODEs defined on the computational mesh [2, 26, 28, 30, 35, 37, 48]. While Eulerian techniques are widely used in fluid dynamics, they are less common for the Vlasov equation. Although the Eulerian framework provides a general procedure for constructing numerical solvers for PDEs, it typically does not exploit the additional structural properties of the system. A well-known plasma gyrokinetic code that is based on an Eulerian description is GENE [34, 36], which uses a mix between pseudospectral and finite-difference approximations to solve the Vlasov part. It has been used in studies of existing experimental devices [6] and in the design of upcoming devices [47].

Because the phase space velocity field of the Vlasov–Poisson equations is divergence-free, characteristics do not cross. Semi-Lagrangian (SL) methods make use of this: they retain a phase-space grid but evolve grid points backward in time for one time step along the characteristic equations, reconstructing the solution at the new time step via interpolation at the characteristic foot [12, 60], which is generally referred to as the *backward Semi-Lagrangian* (BSL) approach. Alternatively, it is also possible to evolve points forward in time, which is called the *forward Semi-Lagrangian* (FSL) method. FSL somewhat simplifies the extension to higher order schemes, however, most Semi-Lagrangian codes still implement the more accurate and stable BSL [18]. The Semi-Lagrangian approach improves conservation properties compared to pure Eulerian schemes, particularly when combined with symplectic time integration. Cubic B-splines are a common choice for interpolation due to their balance between accuracy and efficiency [40, 57], though some codes use nodal interpolation [1, 13, 14, 17, 20, 21, 55, 58, 59]. In this work, we will refer to an SL predictor-corrector scheme using B-splines. It is the basis of Gysela [29] that simulates 5D gyrokinetic equations. It is currently rewritten and generalized for exascale computations [8] using a multi-patch semi-Lagrangian approach [64].

However, there are several drawbacks when using grid-based methods to solve the Vlasov equation. Maintaining a grid of up to six dimensions is extremely costly, especially with adaptivity or non-rectangular domains. The high memory requirements not only severely restrict the maximum possible resolution but also lead to significant communication overhead, which in turn limits parallel efficiency and scalability, especially on modern accelerator hardware such as GPUs [21, 22, 40]. Sparse-grid and adaptive refinements become difficult to deploy in high-dimensional phase space [1, 41]. Moreover, any grid-based discretization introduces numerical diffusion, which reintroduces artificial dissipation into the collisionless Vlasov dynamics and undermines conservation properties. Although several correction techniques exist [17, 28], the effect cannot be completely removed. Grid methods also struggle with irregular geometries, nontrivial boundary conditions, and the need to accommodate growing velocity support.

An alternative to grid-based schemes are particle-based, or Lagrangian, solvers. The most common of these are the *Particle-In-Cell* (PIC) methods, though other approaches exist, such as *smoothed particle hydrodynamics* (SPH) and the *Reproducing Kernel Hilbert Space Particle Method* (RKHS-PM) [7, 15, 33, 68]. The idea behind Lagrangian methods is to approximate the distribution function with a collection of marker particles carrying weights or function values, which are advanced along the phase flow of the Vlasov equation. Since these trajectories coincide with the characteristics of the Vlasov equation, the particle weights remain constant in time—the same principle exploited by Semi-Lagrangian methods. In PIC, a grid in physical space is additionally introduced to solve the Poisson equation for the electric field (or the Maxwell equations for the electro-magnetic case). The charge density, which enters the right-hand side of (2), is then obtained either by counting particles per cell or through higher-order deposition schemes [16, 23, 52, 66]. PIC-based approaches have been widely used in modern gyrokinetic simulations, for example, simulations of Tokamaks like ITER using GTC [65] or Stellarators like W7X using EUTERPE [39].

Like grid-based solvers, PIC is subject to the curse of dimensionality, but it offers important advantages. Particles naturally adapt to evolving dynamics, and the unstructured nature of the data simplifies treatment of complex domains, boundary conditions, and parallelization to distributed computing systems. The main drawback is numerical noise: to achieve the same accuracy as grid-based methods, significantly higher particle counts are required. This becomes problematic in low-density regions or when high accuracy is essential. The majority of implementations are explicit PIC codes [11, 19, 24, 25, 31, 32, 43, 56]. However, due to the strong mass disparity between electrons and ions as well as between the size of individual-particle scales and the domain size, plasma dynamics are highly multi-scale, and explicit schemes demand extremely fine resolution to capture all relevant scales. To address this, fully and semi-implicit PIC methods have been developed [3, 4, 5, 10, 44, 45, 49, 50].

This article combines the versatility and numerical efficiency of Lagrangian solvers with the accuracy of semi-Lagrangian approaches by using a flow map approach. The knowledge of the flow map allows us to trace the characteristics back up to the initial condition, where we can evaluate the distribution function to any given resolution on variable grids. The flow map is generally evolved in a PIC-like manner using the Numerical Flow Iteration method (NuFI) [38]. NuFI has shown high parallel efficiency [38] and versatility concerning boundary conditions, even with low rank approximation [70] and multiple species simulations [67]. Nevertheless, tracing the characteristics backward in time in an iterative manner becomes very costly for long simulations, as for each step forward in time, one additional backward step must be performed in the iterative approach.

An alternative to NuFI is the Characteristic Mapping Method (CMM) [73], which performs remapping by the composition of submaps stored as polynomials. The approach allows for larger time steps backward in time and therefore increases the efficiency when backtracing characteristics. The CMM uses a gradient augmented level set method [53] to advance the submaps further in time. It was originally introduced for the 2D incompressible Euler equations [73], extended to 3D Euler [74] and then has been further generalized for Magneto-Hydro-Dynamics (MHD) [72], shallow water equations [61], and Vlasov–Poisson equations [42].

Contribution

To avoid the time complexity of NuFI, restarting was employed in [70], which, however deteriorates the high-resolution properties of the method. To maintain this, we propose to combine NuFI with CMM. This work therefore contributes: a new flow mapping methodology that reduces the time complexity of NuFI, memory and CPU-time estimations to demonstrate the computational advantage of the combined scheme, and benchmarking on classical test cases, including a comparison with an SL predictor-corrector scheme.

Organization of the Manuscript

The remainder of the manuscript is organized as follows. In section 2 we introduce numerical methods for computing the flow maps, summarizing NuFI in section 2.1 and CMM in section 2.2. The proposed

combination of the two methods is presented in section 2.3. Numerical results for Landau damping and the two-stream instability are shown in section 3. Section 4 concludes and gives some perspectives for future work.

2 Numerical Methods for Calculating Flow Maps

A kinetic equation (KE) describes the evolution of a particle distribution function $f(x, v, t)$ in the phase space $(x, v) \in \mathbb{R}^2$, where x and v denote the canonical position and momentum. In general, KE can be written in the (collisionless) advective form

$$\frac{df}{dt}(\hat{x}(t), \hat{v}(t), t) = \frac{\partial f}{\partial t} + \dot{x}(t) \frac{\partial f}{\partial x} + \dot{v}(t) \frac{\partial f}{\partial v} = 0. \quad (4)$$

Here, the variables $\hat{x}(t)$ and $\hat{v}(t)$ denote the *characteristic trajectories* in phase space, i.e., the solutions of the Hamiltonian equations

$$\dot{x}(t) = \partial_v H(\hat{x}(t), \hat{v}(t)), \quad \dot{v}(t) = -\partial_x H(\hat{x}(t), \hat{v}(t)), \quad (5)$$

with Hamiltonian $H(x, v)$. The initial conditions for these characteristic curves are $(\hat{x}(0), \hat{v}(0)) = (x, v)$. In this work, we consider the 1D+1V Vlasov–Poisson system (VP) with the Hamiltonian $H(x, v) = \frac{1}{2}|v|^2 + q\phi(x)$, $q = 1$. Equation (4) expresses that the distribution function f remains constant along the characteristic curves $(\hat{x}(t), \hat{v}(t))$ defined by (5). The Hamilton flow under which all these trajectories move $\Phi_t^0(x, v) = (\hat{x}(t), \hat{v}(t))$ is volume preserving as a consequence of eq. (5) divergence-free property (Liouville’s Theorem). Thus the solution to eq. (4) can be described by

$$f(x, v, t) = f_0(\Phi_0^t(x, v)), \quad (6)$$

where f_0 is the initial distribution and Φ_0^t the backwards characteristic map. In other words, the knowledge of Φ_0^t inherits all information needed to reconstruct the solution at any phase space position (x, v) .

We remark that the flow map inherits semi-group properties, namely

$$\Phi_t^t = \text{Id}_{\mathbb{R}^2}, \quad \Phi_{t_0}^{t_1} \circ \Phi_{t_1}^{t_2} = \Phi_{t_0}^{t_2}, \quad (\Phi_0^t)^{-1} = \Phi_t^0, \quad (7)$$

which means that the underlying flow Φ_t^0 can be subdivided in the so called submaps:

$$\Phi_0^t = \Phi_0^\tau \circ \Phi_\tau^{2\tau} \circ \dots \circ \Phi_{(n-1)\tau}^{t=n\tau}. \quad (8)$$

The subdivision into two maps is illustrated in fig. 1. The submaps obey the same properties as the backward map. However, they are only defined on subintervals. It was shown previously [42] for the Vlasov–Poisson (VP) equation, that composing the map into submaps and advecting the individual submaps leads to a more efficient representation compared to advecting f itself (see fig. 11 in [42]). This is because Φ does not inherit all the fine-scale properties as present in f . Furthermore, in previous works [42, 73, 74] the submaps Φ have been stored as Hermite polynomials of $p = 3$ order. Thus, making use of the fact that the potentially high-order polynomial representation of Φ can be stored more efficiently as compositions of low-order polynomial Φ . It is essentially this *compositional refinement* that, in contrast to h or p refinement, allows exponential resolution in linear time, enabling the zoom properties shown in fig. 12.

2.1 The Numerical Flow Iteration (NuFI)

A detailed derivation and discussion of the algorithm can be found in previous work [38, 67, 69]. In this section, we want to recap the important ideas and highlight the challenges, which we try to tackle in the following chapters.

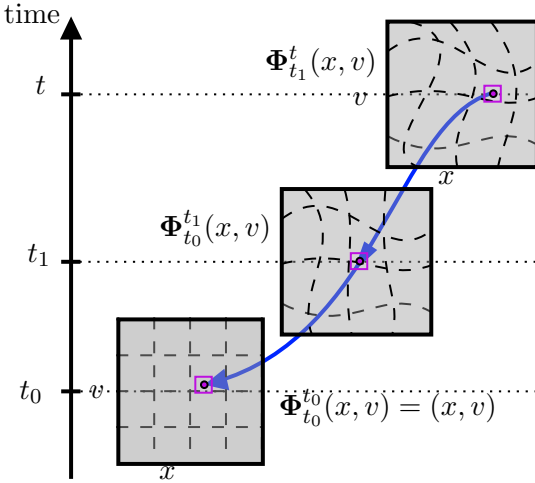


Figure 1: Illustration of the backward map, as a composition of two submaps. The blue line illustrates one characteristic curve.

The core idea of the Numerical Flow Iteration (NuFI) is to approximate the flow map of the Vlasov–Poisson equation iteratively instead of directly solving for and storing the distribution functions f . Therefore, NuFI solves the Hamilton

$$\begin{aligned} \frac{d}{ds} \hat{x}(s) &= -\hat{v}(s), & \hat{x}(t) &= x, \\ \frac{d}{ds} \hat{v}(s) &= E(s, \hat{x}(s)), & \hat{v}(t) &= v. \end{aligned} \quad (9)$$

using the Strömer–Verlet method to advance the maps iteratively backwards in time

$$f(x, v, N\tau) = f_0(\Phi_0^{N\tau}(x, v)) \approx f_0(\Psi_0^{N\tau}(x, v)) \quad (10)$$

$$\text{where } \Psi_0^{N\tau} = \Psi_0^\tau \circ \Psi_\tau^{2\tau} \circ \dots \circ \Psi_{(N-1)\tau}^{N\tau} \quad (11)$$

where each submap $\Psi_{k\tau}^{(k-1)\tau}(x, v)$ is defined by:

$$v_{k-1/2} = v + \frac{\tau}{2} E(x, \tau k), \quad (12)$$

$$x_{k-1} = x - \tau v_{k-1/2}, \quad (13)$$

$$v_{k-1} = v_{k-1/2} + \frac{\tau}{2} E(x_{k-1}, \tau(k-1)) \quad (14)$$

$$\Psi_{(k-1)\tau}^\tau(x, v) := (x_{k-1}, v_{k-1}). \quad (15)$$

According to [38] the introduced error is

$$\|\Phi_0^{N\tau}(x, v) - \Psi_0^{N\tau}(x, v)\|_\infty = \mathcal{O}(\tau^2). \quad (16)$$

Thus, for a smooth initial condition, the error of eq. (10) is given by

$$\|f(x, v, N\tau) - f_0(\Psi_0^{N\tau}(x, v))\|_\infty = \mathcal{O}(\tau^2) \quad (17)$$

Note that to compute $\rho(x, k\tau) \approx 1 - \int f_0(\Psi_0^{k\tau}(x, v))dv$ via (2) we can skip the first half-step (12) as it can be recast as a transformation $\tilde{v} = v + \frac{\tau}{2} E(x, k\tau)$:

$$\int f_0(\tilde{\Psi}_0^{k\tau}(x, v + \frac{\tau}{2} E(x, \tau k)))dv = \int f_0(\tilde{\Psi}_0^{k\tau}(x, \tilde{v}))d\tilde{v} \quad (18)$$

with functional determinant 1. The corresponding NuFI time-stepping algorithm is shown in algorithm 1.

With these components in place, we can outline the full NuFI algorithm for the one-dimensional Vlasov–Poisson system, as depicted in fig. 2. After computing the density ρ , the algorithm obtains

Algorithm 1 NuFI iteration $\text{NuFI}((x, v), [E^{(n)}]_n, \tau, N)$ to evaluate $\Psi_0^t(x, v)$

Input: Position and velocity arrays (x, v) , electric field history $[E^{(k)}]_{k=0}^{N-1}$, time step τ , iteration count N .

Output: Updated position and velocity arrays (x, v) after n steps with half steps.

```

1: if  $n = 0$  then
2:   return  $(x, v)$ 
3: end if
4: while  $n > 0$  do
5:    $n \leftarrow n - 1$ 
6:    $x \leftarrow x - \tau \cdot v$            // Position update (inverse signs, going backwards in time)
7:    $v \leftarrow v + \tau \cdot \mathcal{P}[E^n](x)$  // Velocity update, electric field is interpolated
8: end while
9:  $x \leftarrow x - \tau \cdot v$            // Final position step
10:  $v \leftarrow v + \frac{\tau}{2} \cdot \mathcal{P}[E^0](x)$  // Final half velocity step
11: return  $(x, v)$ 

```

the electric field by solving $\partial_x E = \rho$ in Fourier space. Using the electric fields stored from all previous time steps, NuFI then applies the iterative procedure described in algorithm 1 to trace characteristics back to their initial positions.

To evaluate the electric field at arbitrary spatial locations, an interpolation operator $\mathcal{P}[E^n](x)$ is required. Its construction is detailed in section 2.2, eq. (22). Unless stated otherwise, we employ cubic spline interpolation.

For each query point (x, v) , the iteration in algorithm 1 is carried out, and the corresponding values of f are accumulated to assemble the density field at the next time step.

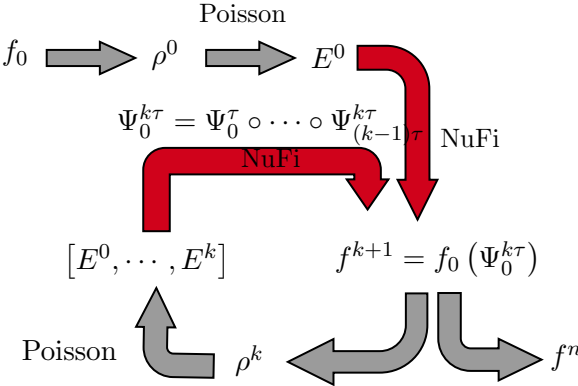


Figure 2: Graphical sketch of the NuFI algorithm. The red arrows indicate the NuFI iteration algorithm 1 at which all (x, v) are evaluated in a streamline fashion, without storing f .

Since for each iteration, only the knowledge of the electric fields $E(t_k, x)$ is necessary, NuFI stores a time series of electric fields to reconstruct the flow map. This turns out to be more memory-efficient than storing f itself, especially in higher dimensions $d = 3$ on stores a set of $N \times 3D$ interpolants $[E_1, \dots, E^N]$ instead of a 6D distribution function f [38]. Nevertheless, it shifts the memory complexity to computational complexity, as for each step forward in time, the number of NuFI iterations to perform backwards in time increases. The complexity in time is therefore increasing quadratically. To reduce this, we propose to combine it with the characteristic mapping method in a hybrid approach that is detailed in section 2.3.

Conservation Properties

We recall the outstanding conservation properties of NuFI proven in [38].

Theorem 2.1. *Let $f(x, v, tN) = f_0(\Psi_0^{N\tau})$ be the discrete solution of NuFI. Then it preserves at all $t = N\tau$:*

- the volume of the flow

$$\det(\nabla_{(x,v)} \Psi_0^{N\tau}(x,v)) = 1 \quad \forall (x,v) \in \mathbb{R} \times \mathbb{R}, \quad (19)$$

- the maximum-principle: $0 \leq f(x,v,N\tau) \leq \|f_0\|_{L^\infty}$,

- kinetic entropy

$$\iint f(x,v,\tau N) \ln(f(x,v,\tau N)) dx dv = \iint f_0 \ln f_0 dx dv, \quad (20)$$

- all integrals for any function $g: \mathbb{R} \rightarrow \mathbb{R}$ of the following form (Liouville's theorem):

$$\iint g(f(x,v,\tau N)) dx dv = \iint g(f_0(x,v)) dv dx. \quad (21)$$

As a consequence of eq. (21) implies the conservation of mass.

We further note that NuFI conserves momentum up to errors made in the spatial discretization of the electric field E [38].

2.2 Characteristic Mapping Method (CMM)

In contrast to NuFI, the characteristic mapping method (CMM) [51] employs compositions based on interpolation to reference back to the initial condition. This more general flow-map framework is not limited to plasma systems but extends to any diffeomorphic flow, including the Euler equations, magnetohydrodynamics and hydrodynamic flows on manifolds [61, 72, 73, 74].

For our numerical experiments we use either Lagrange or spline interpolation on 2D periodic grids \mathcal{G}_χ with an equal number of grid points in each direction $N_\chi \times N_\chi$. Thus, given the grid data points of a map $\Phi_s^t(x_i, v_j), i, j = 1, \dots, N_\chi$, we may represent it in polynomial form:

$$\Phi_s^t(x, v) \approx \chi_s^t(x, v) \equiv P_{\mathcal{G}_\chi}[\Phi_s^t](x, v) = \sum_{i,j} \mathbf{a}_{ij} \cdot b_i(x) \cdot b_j(v), \quad (22)$$

where $b_i(x)$ are either barycentric Lagrange or spline basis elements. Respectively for a Lagrange representation, the coefficients are either $\mathbf{a}_{ij} = \Phi_s^t(x_i, v_j)$, where x_i and v_j are $m+1$ nearby nodes around the evaluation points (x, v) or spline coefficients \mathbf{a}_{ij} as a result of solving a linear spline systems. Depending on the polynomial order m the approximation error introduced is thus:

$$\|\Phi_s^t - \chi_s^t\|_\infty \leq c \max_{(x,v)} \frac{\|\nabla_{(x,v)}^{(m+1)} \Phi_s^t(x, v)\|}{(m+1)!} h^{m+1}. \quad (23)$$

In earlier works [42], the backwards map was advanced by a semi-Lagrangian scheme known as the gradient-augmented level set method (GALS) [53]. GALS solves

$$\chi_0^t: \begin{cases} \partial_t \chi + \mathbf{u} \cdot \nabla \chi &= 0 \\ \chi(x, v, 0) &= (x, v) \end{cases} \quad \text{with} \quad \mathbf{u}(x, v) = (v, E(x, t)) \quad (24)$$

backwards in time, which is equivalent to solving eq. (5). Note, to update the electric field $\partial_x E = \int f dv$ we always have to map back to the initial condition: $f(x, v, t) = f_0(\chi(x, v, t))$. However, unlike NuFI, GALS is not symplectic and therefore introduces an incompressibility error,

$$\epsilon_{\text{incomp}} = |\det(\nabla \chi) - 1|, . \quad (25)$$

As demonstrated for 2D Euler [71, p.22], this error can induce overshooting, wherein characteristics become too close or cross, compromising the map's injectivity. To control such deviations, a remapping procedure is employed: whenever a map $\chi_{t_{i-1}}^{t_i}$ violates a prescribed incompressibility threshold δ_ϵ , i.e.,

$\epsilon_{\text{incomp}} > \delta_\epsilon$, a new map is generated and composed with the preceding maps whenever one needs to access the full map. We thus exploit the semi-group property eq. (7) of the characteristic map:

$$\chi_{t_{i-1}}^{t_i} : \begin{cases} \partial_t \chi + \mathbf{u} \cdot \nabla \chi = 0 & \text{for } t \in [t_{i-1}, t_i] \\ \chi(x, v, t_{i-1}) = (x, v) \end{cases} \quad \text{with} \quad (26)$$

$$f(x, v, t) = f_0(\chi_{t_0}^t(x, v)) \text{ and } \chi_{t_0}^t = \chi_{t_0}^{t_1} \circ \chi_{t_1}^{t_2} \circ \cdots \circ \chi_{t_{m-2}}^{t_{m-1}} \circ \chi_{t_{m-1}}^t. \quad (27)$$

Remark 1. We remark that even for a symplectic scheme (such as NuFI) eq. (25) will not vanish in most cases, since the finite representation errors of the map will show up in the higher order terms of the approximated derivatives. In other words, eq. (25) not only measures the compressibility but the representation quality of the map in general. This is intuitively clear as two arbitrarily close characteristics may not be representable on a finite grid. This fact is visualized for the consecutive compositions of the volume-preserving submap

$$\Phi(x, v) = (x + \sin(\pi v), v) \quad (28)$$

in fig. 3. Although the approximation error decreases with fourth order for our chosen 4th order Lagrangian interpolation scheme. The incompressibility error remains and increases with the increasing number of map decompositions.

Similarly to NuFI, the characteristic map allows provides exponential resolution in linear memory, because the compositional structure allows for representing exponentially high order polynomials with a linear increase in the number of coefficients.

Example 1. If each map is a cubic polynomial $\chi_{t_{i-1}}^{t_i} \in P_3$, then

$$\chi_{t_0}^t = \chi_{t_0}^{t_1} \circ \cdots \circ \chi_{t_{m-1}}^t \in P_3 \circ \cdots \circ P_3 \subset P_{3^m} \quad (29)$$

Represents an element of P_{3^m} ($3^m + 1$ coefficients), by storing $(3 + 1) \cdot m$ coefficients of P_3 .

As a consequence, the maps can be stored on a coarse grid \mathcal{G}_χ with $N_\chi \times N_\chi$ coefficients. To circumvent the high dimensionality, one can later evaluate $\rho(x) = \int f(\chi_{t_0}^t(x, v)) dv$ pointwise in a fast way on any sample grid \mathcal{G}_f that is fine enough to represent the solution well. This effectively avoids storing f in the active memory, as f can be evaluated in a streamlined fashion using the compositional structure eq. (27).

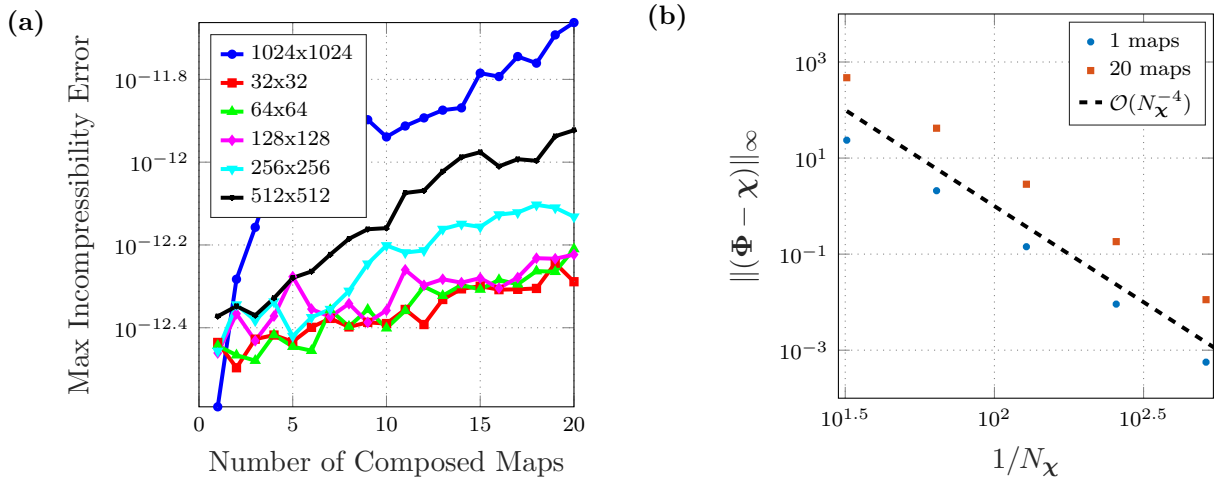


Figure 3: Incompressibility error using Lagrange interpolation. a) maximum error as a function of the number of maps. b): Decay of the L_∞ -error as a function of the map grid resolution N_χ .

2.3 Hybrid CMM-NuFI method

The proposed semi-Lagrangian flow map approach combines NuFI (section 2.1) and CMM (section 2.2). The idea is visualized in fig. 4 and the algorithm detailed in algorithms 3 and 4. Depending on the remapping strategy, the solution is locally evolved using NuFI iterations and after a

Algorithm 2 Numerical composition of maps `compose_maps`($[\chi^{(k)}]_{k=1}^M, (\mathbf{X}, \mathbf{V})$)

Input: Maps $[\chi^{(k)}]_{k=1,\dots,M}$ (4D array $N_\chi \times N_\chi \times 2 \times M$), coarse grid \mathcal{G}_χ at which map is stored, (\mathbf{X}, \mathbf{V}) query coordinates to evaluate the maps on

Output: Composed map $\chi_{\text{cmm}}(x, v) = \chi_{t_0}^{t_1} \circ \dots \circ \chi_{t_{M-1}}^{t_M}(x, v)$

- 1: **for** $i = M, \dots, 1$ **do**
- 2: $\Delta\chi^{(i)} \leftarrow \chi^{(i)} - (\mathbf{X}_{\mathcal{G}_\chi}, \mathbf{V}_{\mathcal{G}_\chi})$ *// Compute deviation of map i around the identity*
- 3: $(\Delta\mathbf{X}, \Delta\mathbf{V}) \leftarrow \mathcal{P}_{\Delta\chi^{(i)}}(\mathbf{X}, \mathbf{V})$ *// Interpolate displacement fields at query points*
- 4: $\mathbf{X} \leftarrow \mathbf{X} + \Delta\mathbf{X}$ *// Apply transformation:*
- 5: $\mathbf{V} \leftarrow \mathbf{V} + \Delta\mathbf{V}$ *// new point = old point + displacement*
- 6: **end for**
- 7: **return** (\mathbf{X}, \mathbf{V}) *// Return final composed map*

certain number of iterations N the generated iterative map $\Psi_{t_i}^{t_i+N\tau}$ is replaced by a stored submap $\chi_{t_i}^{t_{i+1}}$, $t_{i+1} = t_i + N\tau$. The number of NuFI iterations N can be either chosen statically by a remapping frequency or adapted to the solution itself as suggested in [73]. In this work, we only make use of manual remapping, as we are interested in optimizing the time complexity of NuFI. Hence, to

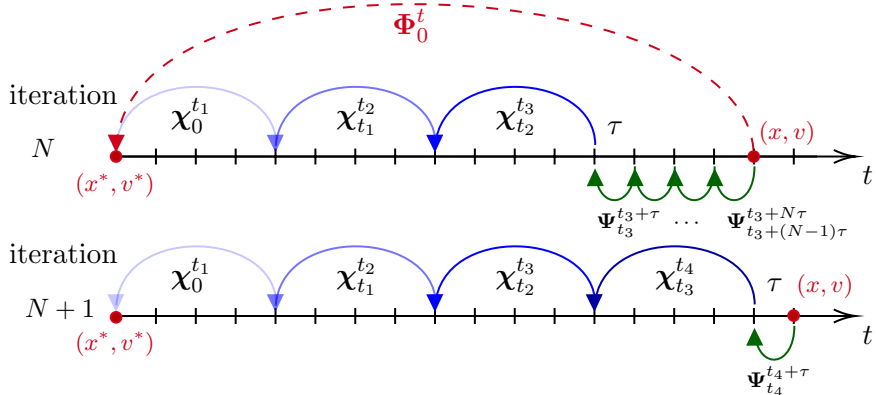


Figure 4: Schematic of the backward flow $(x^*, v^*) = \Phi_0^t(x, v)$ for two consecutive iterations with the hybrid CMM-NuFI method. Given a point in phase space (x, v) , the characteristics are traced back to their footpoints (x^*, v^*) using an iterative flowmaps Ψ (green arrows) and compositional flowmaps χ (blue arrows). The two consecutive iterations visualize the remapping. After four NuFI steps (green), the resulting map is replaced in the next iteration by a single large submap (dark blue) and concatenated with the rest of the submaps.

represent the solution $f(x, v, t)$ at time $t = t_M + N\tau$ after M remappings and N NuFI iterations, we use the following decomposition:

$$f(x, v, t) = f_0(\Phi_0^t(x, v)), \quad \text{where} \quad (30)$$

$$\Phi_0^t \approx \tilde{\Phi}_0^t := \underbrace{\chi_0^{t_1} \circ \chi_{t_1}^{t_2} \circ \dots \circ \chi_{t_{M-1}}^{t_M}}_{=\chi_{\text{CMM}}} \circ \underbrace{\Psi_{t_M}^{t_M+\tau} \circ \Psi_{t_M+\tau}^{t_M+2\tau} \circ \dots \circ \Psi_{t_M+(N-1)\tau}^{t_M+N\tau}}_{=\Psi_{\text{NuFi}}}. \quad (31)$$

The convergence order of the hybrid method $\tilde{\Phi}_0^t := \chi_{\text{CMM}} \circ \Psi_{\text{NuFi}}$ is given by the time error $\mathcal{O}(\tau^2)$ coming from Ψ_{NuFi} and the interpolation errors $\mathcal{O}(1/N_\chi^\alpha)$ of χ_{CMM} :

$$\|\Phi_0^t - \tilde{\Phi}_0^t\|_\infty = \mathcal{O}(\tau^2) + \mathcal{O}(1/N_\chi^\alpha). \quad (32)$$

Same holds for the solution $\|f_0(\Phi_0^t) - f_0(\tilde{\Phi}_0^t)\|_\infty$ if the initial condition f_0 is sufficiently smooth. The spatial convergence of our scheme is visualized for the Landau damping in fig. 5.

In the proposed scheme, we use NuFI for local time stepping with step size τ and the CMM submap composition algorithm 2 to relate back the solution to the initial footpoints. Note, that the NuFI

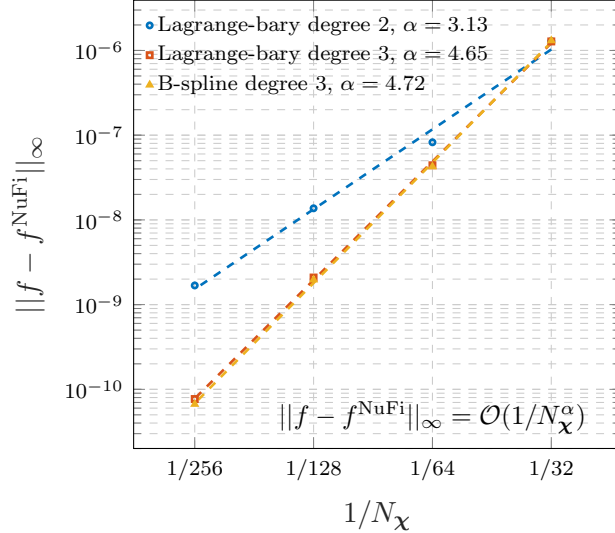


Figure 5: Spatial convergence for the Landau damping test case at $T = 2$ with $\tau = 0.1$ using different interpolation schemes. The reference solution is pure NuFI with a spatial resolution $N_f = 512$.

Algorithm 3 NuFI half step adjusted NuFI_adj($(x, v), [E^{(n)}]_n, \tau, N$)

Input: Position and velocity arrays (x, v) , electric field history $[E^{(k)}]_{k=0}^{N-1}$, time step τ , iteration count N .

Output: Footpoints (x, v) going back in time $N\tau$.

```

1: if  $n = 0$  then
2:   return  $(x, v)$ 
3: end if
4: if  $N_{\text{maps}} = 0$  then
5:    $(x, v) = \text{NuFI}((x, v), [E^{(n)}]_n, \tau, N)$ 
6: else
7:   while  $n > 1$  do
8:      $n \leftarrow n - 1$ 
9:      $x \leftarrow x - \tau v$ 
10:     $v \leftarrow v + \tau \mathcal{P}[E^n](x)$ 
11:   end while
12: end if
13: return  $(x, v)$ 

```

algorithm 3 has to be adapted for $M > 1$, avoiding the final half step for consistency with the previous maps.

Summarizing multiple NuFI steps into a big CMM step with step size $\Delta t = N\tau$ allows us to reduce NuFI's quadratic complexity in time by several orders of magnitude. This is shown in fig. 10 for the cumulative CPU time, where we compare the hybrid scheme against NuFI using different remapping frequencies N_{remap} . The typical behavior of the hybrid method can be observed, where the complexity per iteration of the method decreases, as fewer NuFI iterations are required per time step. This resetting of complexity creates a sawtooth function in fig. 10, resulting in a reduction of the overall CPU time by several orders of magnitude. This complexity reduction enables us to run much longer plasma simulations. Further note that a sweet spot between iterative and compositional mapping is achieved for $N_{\text{remap}} = 20$ iterations between remappings. This sweet spot is reached when the complexity of the map iteration and composition is equal, $t_{\text{CPU}}(\Phi_{\text{CMM}}) = t_{\text{CPU}}(\Psi_{\text{NuFi}})$. It might be dependent on the parallelization strategy of the NuFI iterations and CMM compositions, the problem size, and the length of the simulation, which affects the total number of CMM map compositions. As in the original CMM method section 2.2 we store χ on a coarse grid \mathcal{G}_χ for computational efficiency. Therefore we only store $N_\chi \ll N_f$ sample points when performing remapping in algorithm 4 line 9.

Algorithm 4 Hybrid CMM-NuFI time step CMM-NuFI($[\chi^{(k)}]_k, [E^{(n)}]_n, \tau$)

Input: Submaps $[\chi^{(k)}]_{k=1,\dots,M}$ Electric field $[E^{(n)}]_{n=1,\dots,N}$, time step τ .
Output: Updated map list $[\chi^{(k)}]_k$ and electric field list $[E^{(n)}]_n$.

```

1:  $N \leftarrow N + 1$  // increase NuFI iteration counter
2: Initialize:
    $X_{ij} = i\Delta x$ ,
    $V_{ij} = j\Delta v - L_v/2$  for  $i, j = 1, \dots, N_f$  // Sample Grid  $N_f$ 
3:  $(X, V) = \text{NuFI\_adj}((X, V), [E^{(n)}]_n, \tau, N)$  // implements  $\Psi_{t_M}^{t_M+N\tau}$ 
4:  $(X^*, V^*) = \text{MapsCompose}([\chi^{(k)}], (X, V))$  // Implements composition of maps
5:  $f^{\text{new}}(X, V) = f_0(X^*, V^*)$  // Compose with initial condition
6: Compute Density  $\rho = \int f^{\text{(new)}} dv - 1$ 
7: if  $N \bmod N_{\text{remap}} = 0$  then
8:    $M \leftarrow M + 1$ 
9:    $\chi^M = \text{down\_sample}(X, V, \mathcal{G}_\chi)$  // add coarse submap to  $[\chi^{(k)}]$ 
10:   $N \leftarrow 1$  // reset NuFI iteration counter
11: end if
12: Solve Poisson:  $\nabla^2 \phi = \rho$ 
13: Set  $E^{(N)} = -\nabla \phi$ 

```

Memory and Computational Complexity

For estimating the computational costs, we assume that the initial condition f_0 is given analytically and therefore does not require memory. Furthermore, we assume that the sampling and map grid are resolved with the same number of grid points in x and v direction $N_v = N_x$. However, the resolution of the sampling grid and map grid are different $N_\chi \leq N_f$. Furthermore, we assume that the electric field is stored on the fine sample grid \mathcal{G}_f , which might not be necessary, as it is a smooth function. Following [38], the memory usage is given by:

$$\text{Memory NuFI} = (N + 1)N_f^d \times 8 \text{ bytes.} \quad (33)$$

in terms of the dimension d (in this study $d = 1$). Similarly, the storage for M CMM maps is

$$\text{Memory CMM} = (M)2dN_\chi^{2d} \times 8 \text{ bytes.} \quad (34)$$

Choosing $M = \lfloor \frac{N}{N_{\text{remap}}} \rfloor$ where N is assumed to be the total iteration number, we can deduce the hybrid memory storage as:

$$\text{Memory CMM-NuFI} = \left[(M)2dN_\chi^{2d} + (N - MN_{\text{remap}} + 1)N_f^d \right] \times 8 \text{ bytes.} \quad (35)$$

In fig. 6 we plot the memory consumption of NuFI vs. the number of iterations and compare it to the hybrid approach for different remapping frequencies N_{remap} , map grid resolutions N_χ . It can be seen that the memory consumption of both schemes increases per iteration. The slope of the memory increase is influenced by the dimensionality and grid resolution. The typical sawtooth structure of the memory consumption is best visible for the configuration ($N_{\text{remap}} = 100, N_\chi = 64, d = 1$) in fig. 6. The sawtooth is due to the remapping, which shifts the storage of electric fields E to the storage of maps χ .

In the same manner for the computational complexity, NuFI's cost scales as [38]:

$$\text{Cost NuFI} = N_f^{2d} \sum_{k=1}^N (k + 1) = N_f^{2d} (N + 3) \frac{N}{2}. \quad (36)$$

assuming that NuFI is evaluated at the sampling grid \mathcal{G}_f . The costs for interpolating submaps depend on the interpolation scheme. Here we assume that the costs for evaluating the polynomial of order α is dominant over the setup of the coefficients and compose M CMM maps

$$\text{Cost CMM composition} = [(\alpha + 1)N_f]^{2d} \times M. \quad (37)$$

Choosing as before $M = \lfloor \frac{N}{N_{\text{remap}}} \rfloor$, with N the total iteration number, we can deduce the hybrid computational complexity as:

$$\text{Cost CMM-NuFI} = N_f^{2d} [(N - MN_{\text{remap}} + 3) \frac{N - MN_{\text{remap}}}{2} + (\alpha + 1)^{2d} \times M]. \quad (38)$$

For a typical example like Landau damping, the computational costs are plotted in fig. 10. It can be seen that the cumulative CPU time scales quadratically both for NuFI and CMM-NuFI, however, the slope is reduced in the hybrid method.

3 Results

In the following section, we benchmark the proposed hybrid method using two classical test cases: linear Landau Damping in section 3.1 and two-stream instability in section 3.2. For our comparison, we recall the conserved properties that we studied in our test cases in a solution domain $\Omega_x \times \Omega_v$. These are the *mass* (*0. moment*)

$$\mathcal{M}(t) = \int_{\Omega_x} \rho(x, t) dx = \iint_{\Omega_x \times \Omega_v} f(x, v, t) dx dv, \quad (39)$$

and its *moment* (*1. moment*)

$$\mathcal{P}(t) = \int_{\Omega_x} j(x, t) dx = \iint_{\Omega_x \times \Omega_v} vf(x, v, t) dx dv. \quad (40)$$

Furthermore, the *total energy* is conserved

$$\mathcal{E}(t) = \mathcal{E}_{\text{pot}}(t) + \mathcal{E}_{\text{kin}}(t), \quad (41)$$

which is the sum of *kinetic energy*

$$\mathcal{E}_{\text{kin}}(t) = \frac{1}{2} \int_{\Omega_v} \int_{\Omega_x} f(x, v, t) |v|^2 dx dv, \quad (42)$$

and *potential energy*

$$\mathcal{E}_{\text{pot}}(t) = \frac{1}{2} \int_{\Omega_x} |E(x, t)|^2 dx = \frac{1}{2} \int \int_{\Omega_x} \rho(t, x) \phi(t, x) dx. \quad (43)$$

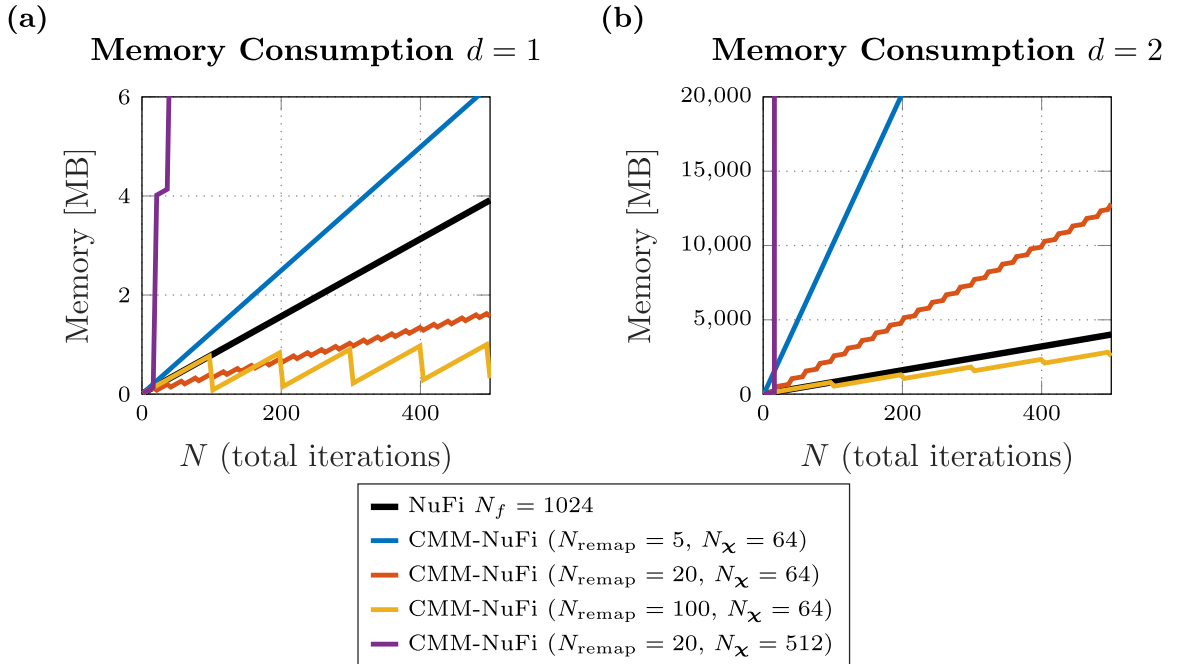


Figure 6: Memory vs iteration for various grid resolutions N_x , remapping frequencies N_{remap} and dimensionality $d = 1, 2$. For all examples, the sample grid resolution is $N_f = 1024$.

3.1 Landau Damping

Here we study linear Landau damping for 1D+1V Vlasov–Poisson equation with a perturbed Maxwellian distribution as initial condition:

$$f_0(x, v) = (1 + \epsilon \cos(kx)) \frac{1}{\sqrt{2\pi}} e^{-v^2/2} \quad \text{with } \epsilon = 0.01, k = 0.5. \quad (44)$$

For time stepping, we use $\tau = 0.1$ and a constant remapping frequency of $N_{\text{remap}} = 20$. For the numerical discretization of the CMM maps, we use Lagrange interpolation of 3rd order with an equal number of N_χ grid points in each direction. The distribution function f is sampled using N_f grid points in each dimension. Thus, the electric fields and the density are represented on N_f points.

Damping rate

In fig. 7, we compare the previously developed NuFI method [38] with the proposed method concerning the decay of the potential energy and compare it to the theoretical prediction. For all different

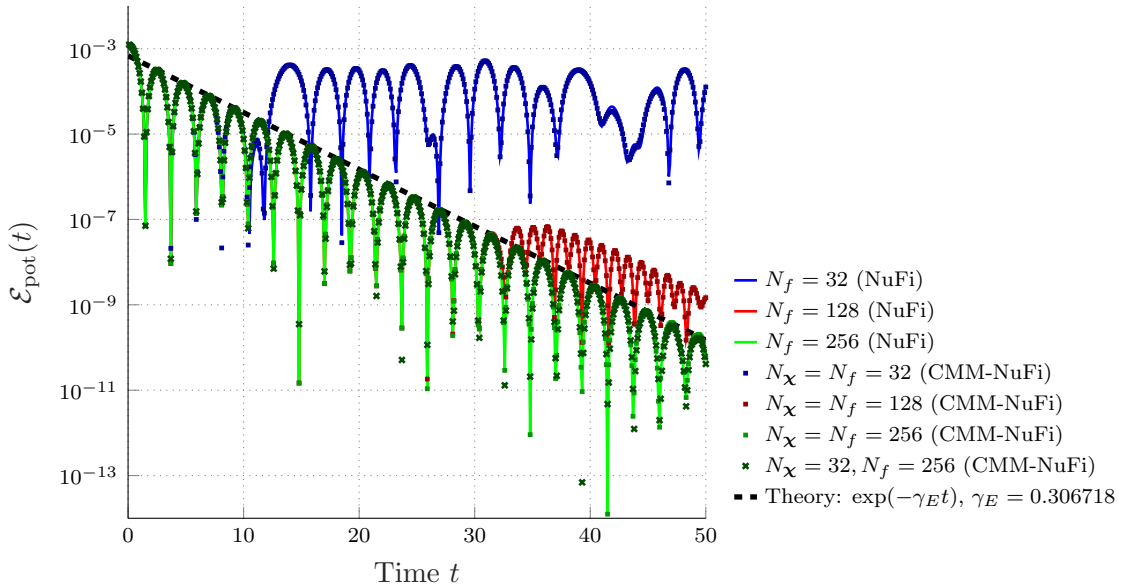


Figure 7: Linear Landau damping for NuFI and CMM-NuFI studied for different sample grid resolutions N_f and map grid resolutions N_χ , time step $\tau = 0.1$ and remapping frequency $N_{\text{remap}} = 20$ for CMM-NuFI.

resolutions studied, we see perfect overlap of the decay of the potential energy for both methods. Similarly to the observations in [38, 42] we observe that increasing the number of sampling grid points allows us to resolve lower potential energies. This is due to the filamentations that need to be resolved when solving the Poisson equation. Moreover, we note that the resolution of the map grid does not have visible influence on the evolution of \mathcal{E}_{pot} shown in fig. 7. A map grid with $N_\chi = 32$ points combined with a sample grid with $N_f = 256$ produces indistinguishable results from a simulation in which both grids use the same resolution, $\mathcal{G}_\chi = \mathcal{G}_f$ with $N_\chi = N_f = 256$. This behavior is consistent with the findings reported in [42].

Conservational Properties

The conservation of mass, momentum, total energy and the L_2 -norm of the distribution function have been tested and compared in fig. 8 against the previously developed CMM method [42], that is, using the gradient augmented level-set method [53] to solve eq. (27), NuFI [38] and a classical backward semi-Lagrangian predictor-corrector method detailed in [9].

Additionally, we show the time evolution of the incompressibility error eq. (25) in fig. 9. If not

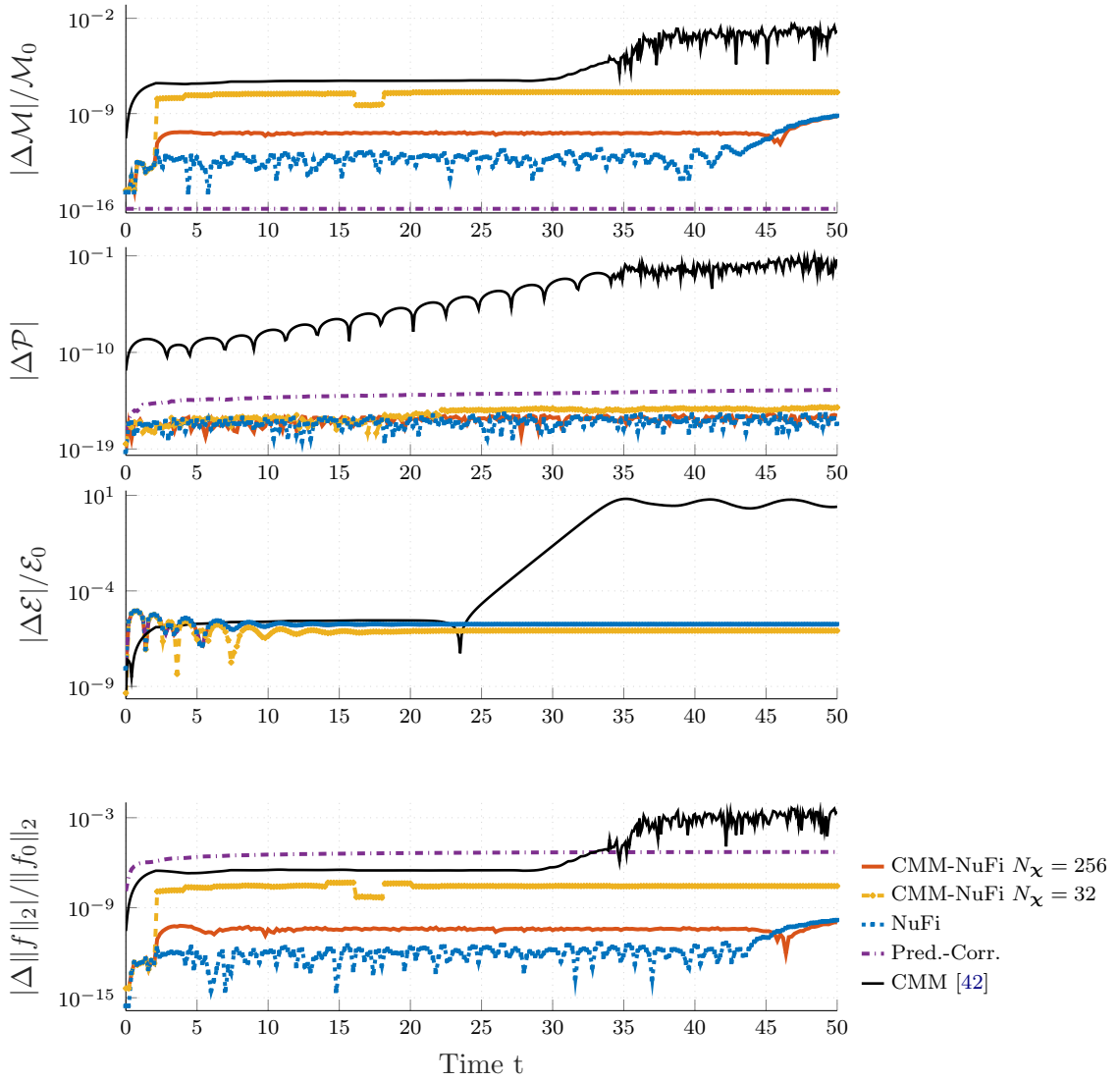


Figure 8: Conservation for Landau damping using a sample grid with $N_f = 256$ and time step $\tau = 0.1$. For the CMM method, we use adaptive remapping with incompressibility threshold (incomp. threshold) $\delta_\epsilon = 10^{-2}$, i.e., $\epsilon_{\text{incomp}} < \delta_\epsilon$, and CMM-NuFI is remapped after $N_{\text{remap}} = 20$ NuFI iterations.

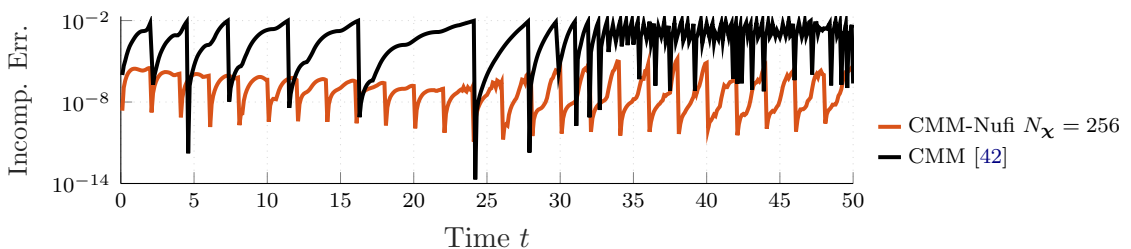


Figure 9: Incompressibility error for Landau damping using a sample grid with $N_f = 256$ and time step $\tau = 0.1$. For the CMM method, we use adaptive remapping $\epsilon_{\text{incomp}} < 10^{-2}$ and CMM-NuFI is remapped after $N_{\text{remap}} = 20$ NuFI iterations.

otherwise stated, we use Lagrange interpolation of 3rd order for all three methods, time step $\tau = 0.1$, and a sampling grid size of $N_f = 256$ in each dimension x, v .

The time evolution of the difference with the initial condition shows that the hybrid CMM-NuFI and the classical NuFI methods overlap before the first remapping. After introducing the first CMM map, small deviations between the two methods are visible in the mass and L_2 conservation, which can be explained as the interpolation scheme is not volume preserving. Similarly, increasing the introduced interpolation error with a coarser map resolution (here $N_\chi = 32$) leads to larger errors in the volume preservation, which can be seen in the mass and L_2 conservation. These errors jump when a CMM map is introduced, as can be seen when comparing the remapping intervals in fig. 9 with the jumps in mass conservation, fig. 8 around $t = 15$. Nevertheless, we observe an advantage over the classical CMM method, which is expected as the GALS is not volume preserving. Comparing the flow-mapping methods with the predictor-corrector scheme, we see that the 3rd order predictor-corrector outperforms the others concerning mass conservation. On the other side, the flow mapping methods show several orders of magnitude better preservation of the L_2 -norm.

Performance Improvements

Besides improving the conservation properties of the classical CMM approach, the hybrid method outperforms NuFI concerning computational efficiency. This is graphically visualized in fig. 10 for the CPU time per iteration and cumulative CPU time. We use a sample grid size of $N_f = 256$ and a time step size of $\tau = 0.1$. Depending on the remapping frequency N_{remap} , we observe different behavior of our method. If no remapping is performed (plain NuFI), the CPU time per iteration increases linearly with time, as for each new time step, an additional backward step is necessary. This results in a quadratic increase in the cumulative CPU time, visible in fig. 10b for the NuFI iteration. If we introduce remapping, the CPU time per iteration decreases drastically as the number of NuFI iterations is replaced by an interpolation. The characteristic sawtooth structure is shown for $N_{\text{remap}} = 10 - 40$. If we remap rapidly with $N_{\text{remap}} = 5$ we also see a linear increase in CPU time, which is due to the increasing number of compositions to construct the CMM backward map using interpolation. Although the resulting slope for a low remapping frequency is also quadratic, it is less steep as pure NuFI. The slope of the two extremes depends on the software realization, size of the grids (N_f, N_χ) and dimension of the problem. Nevertheless, for our test case, we found that $N_{\text{remap}} = 20$ gives the best compromise between performance and introduced incompressibility error shown in fig. 9. For the Landau damping presented here, we observe that the cumulative CPU time is indeed the lowest for $N_{\text{remap}} = 20$ at $t = 40$.

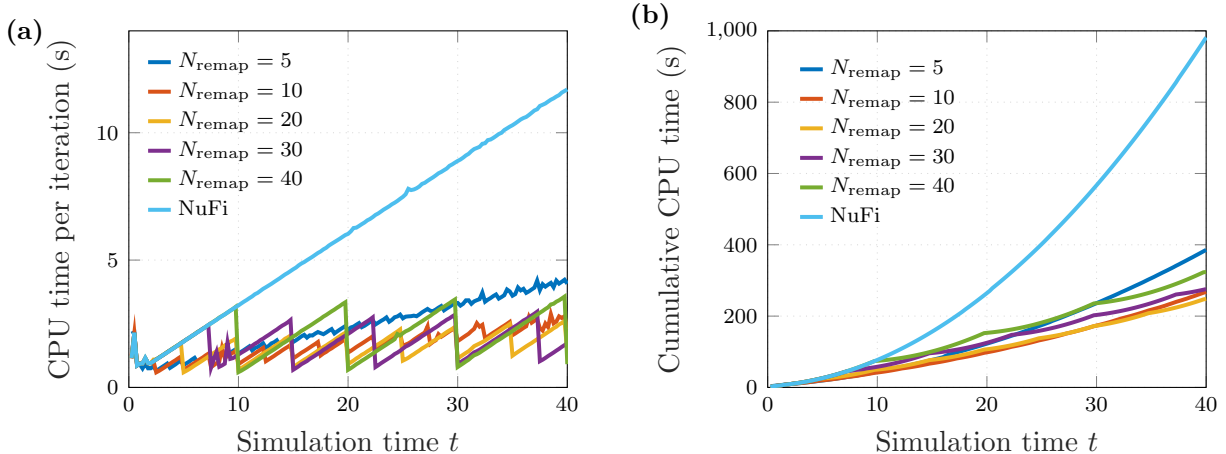


Figure 10: CPU time per iteration (a) and cumulative CPU time (b) using a sample grid with $N_f = 256$ and time step $\tau = 0.1$. Simulations have been performed on ARM64.

Spatial Convergence

The convergence of our scheme is studied in fig. 5 for different grid resolutions $N_\chi = N_f = 32, 64, 128, 256$ and interpolation schemes to confirm eq. (32). In fig. 5 we upsample the solution of the NuFI-CMM simulations to our reference solution grid 512×512 that is computed with NuFI and we calculate the maximums error. To minimize the time error, we use for both the reference and the CMM-NuFI simulation a small time step size of $\tau = 0.01$ and we compare our solution at $T = 10$. The remapping frequency was chosen as before $N_{\text{remap}} = 20$.

3.2 Two-stream instability

The two-stream instability is a classical test case for studying fine-scale behavior in phase space. The initial condition is given by

$$f_0(x, v) = (1 + \epsilon \cos(kx)) \frac{1}{2\sqrt{2\pi}} (e^{-(v-v_0)^2/2} + e^{-(v+v_0)^2/2}) \quad \text{with } \epsilon = 0.05, k = 0.2, v_0 = 3. \quad (45)$$

We compare the evolution of the potential energy for the three different schemes in fig. 11. To this end, we use for all the schemes a time step of $\tau = 0.2$. Furthermore, remapping is performed in the CMM-NuFI method after $N_{\text{remap}} = 20$ NuFI steps. As reported in [70], we observe diffusive behavior of the classical semi-Lagrangian scheme, which implies a variation of the total amplitude (maximum principle in theorem 2.1) and results in a decay of the potential energy over time. This is especially pronounced in the linear predictor-corrector visualized in fig. 11. As in the Landau damping case shown in fig. 7, we see no change in the potential energy when varying the mapgrid resolution N_χ ($N_\chi < N_f$) or when using different interpolation orders.

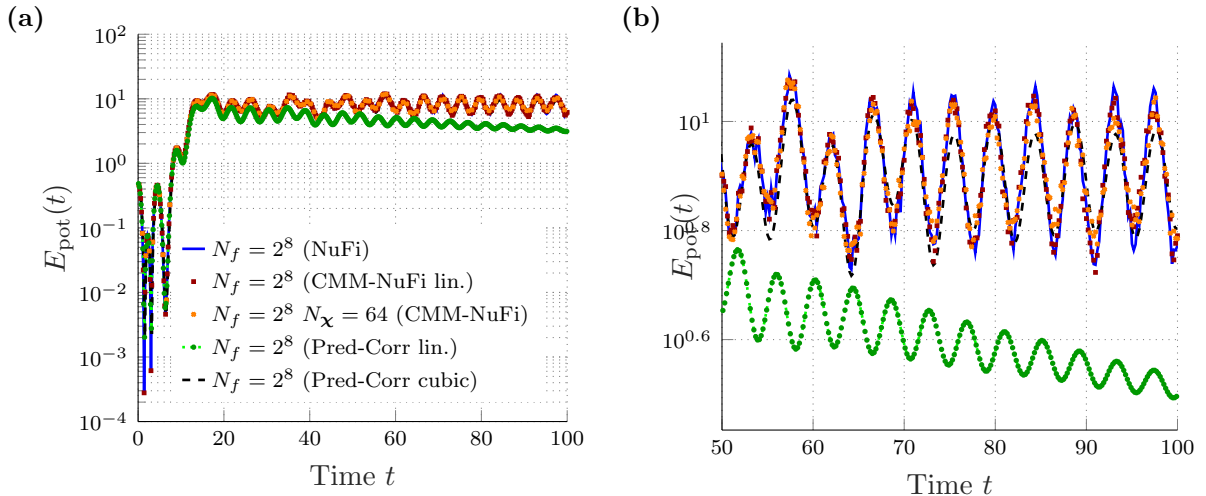


Figure 11: Evolution of the potential energy as a function of time for NuFI, CMM-NuFI and the predictor-corrector scheme (a) and a zoom in the non-linear regime (b).

To visualize the fine-scale properties, we have plotted the solution at $t = 100$ for the different methods in fig. 12. Comparing the flow map methods with the classical semi-Lagrangian representation, we estimate a storage of 3.9MB for NuFI, storing 500 electric field vectors $E^k \in \mathbb{R}^{N_f}, N_f = 1024$, 0.8MB for CMM-NuFI storing 25 maps of size 64×64 , and the predictor-corrector scheme 8MB for the point values of f on a 1024×1024 sample grid. We see that less memory is needed in order to resolve the solution. Further, as shown in fig. 12 the flow mapping approach allows us to zoom into the solution to access its fine-scale properties, which are lost for the classical predictor-corrector semi-Lagrangian scheme. Additionally, the initial range is not preserved by the predictor-corrector scheme, as a consequence of its diffusivity. The conservation of mass, momentum and energy is shown for the three simulations in fig. 13. We note that, in contrast to fig. 8, the simulation of the two-stream instability using the older CMM [42] shows less of a discrepancy in the conservation errors relative to the other methods than in the Landau damping case.

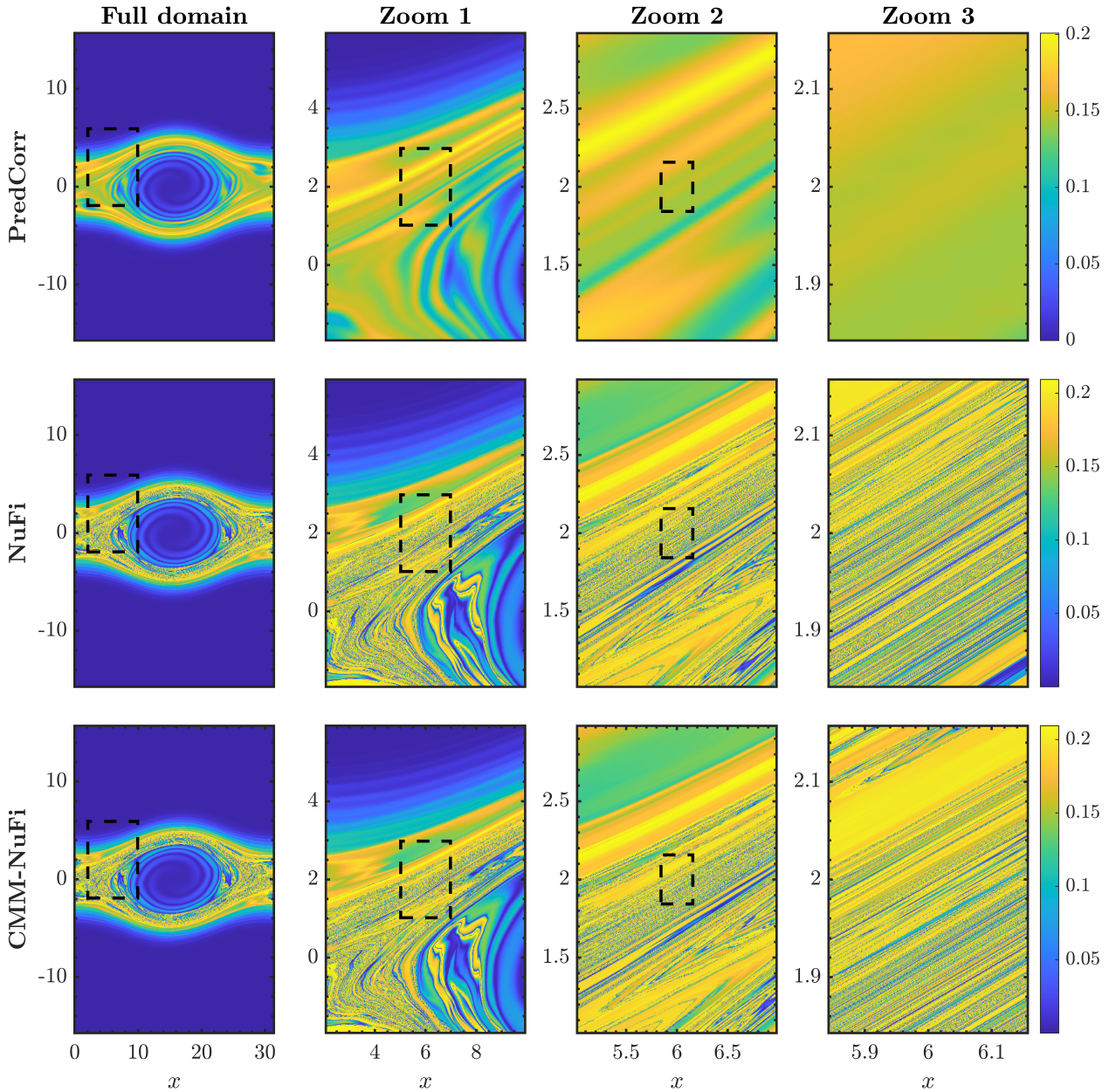


Figure 12: Zoom properties for the two-stream instability at $t = 100$. We compare three zooms: NuFi, CMM-NuFi, and the predictor-corrector scheme. Each zoom is evaluated on a 1024×1024 grid. The results from the predictor-corrector simulation are interpolated inside the zoom windows using cubic splines.

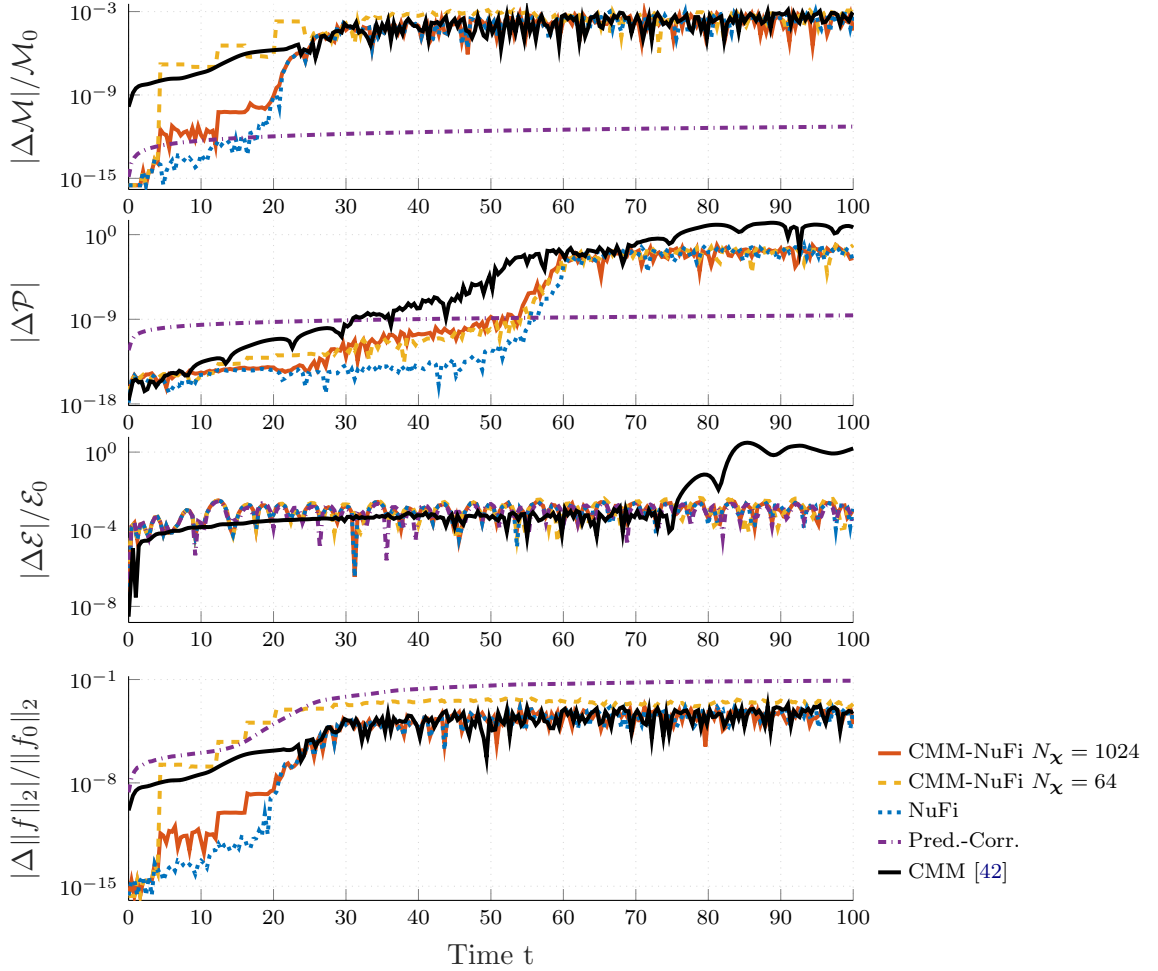


Figure 13: Conservation errors for the two-stream instability test case using a sample grid with $N_f = 1024$. For the CMM method, we use adaptive remapping with incomp. threshold $\delta_\epsilon = 10^{-2}$ (i.e., $\epsilon_{\text{incomp}} < \delta_\epsilon$) and CMM-NuFI is remapped after $N_{\text{remap}} = 20$ NuFI iterations. All simulations use the same time step size of $\tau = 0.2$.

4 Conclusion

We have presented a hybrid flow mapping approach that merges the Characteristic Mapping Method (CMM) and Numerical Flow Iteration (NuFI) to compute the backward map for the Vlasov–Poisson equation. By integrating CMM’s efficient backmapping with NuFI’s accurate time-stepping, our method achieves enhanced conservation properties over CMM [42] and accelerates performance by orders of magnitude over NuFI [38]. This enhanced performance enables high-resolution, long-duration simulations illustrated for different test-cases in 1D+1V.

Benchmarking against a semi-Lagrangian predictor-corrector scheme reveals improvements in the L_2 and maximum norms, as well as in momentum conservation. Importantly, the method uses the semigroup property of diffeomorphic flow maps to break down the flow into a sequence of submaps. This approach means memory needs grow linearly, but resolution improves exponentially compared to standard semi-Lagrangian schemes. We can thus “zoom in” to achieve extremely fine resolution, revealing small-scale details that are important for problems like plasma filamentation and for simulations in higher dimensions. The fine-scale structures resolved in the two-stream instability distribution functions underscore this capability.

This hybrid framework opens several promising research avenues. Future work will focus on incorporating source terms, following the approach established for CMM [72], to enable the simulation of collisional kinetic systems. Furthermore, we plan to generalize the method to handle boundary conditions, as demonstrated in NuFI, and to implement low-rank compression of the CMM maps [70] to ensure memory efficiency for high-dimensional plasma simulations.

Author Contribution Statement

The following outlines the authors’ contributions to this work. Z. Lin and P. Krah contributed equally as first authors.

P. Krah:	Conceptualization, Methodology, Investigation, Implementation, Software, Validation, Visualization, Writing original draft,
Z. Lin:	Implementation, Visualization, Numerical Simulations, Writing – original draft,
F. Bacchini:	Review & editing, Funding acquisition.
P. Wilhelm:	Numerical Simulations, Writing original draft, Review and Editing,
J.-C. Nave	Review & Editing, Funding acquisition,
V. Grandgirard	Review & Editing, Supervision of P.Krah, Funding acquisition,
K. Schneider:	Writing original draft, Review & Editing, Funding acquisition, supervision.

Code Availability

The code will be made publicly available upon publication.

Acknowledgments

The authors thank Xi Yuan Yin and William Holman-Besinger for fruitful discussions. This work was supported by the Institute for Fusion Sciences and Instrumentation in Nuclear Environments (ISFIN) at Aix-Marseille Université, funded by the French government under the France 2030 program managed by the A*MIDEX initiative (AMX-19-IET-013). Additional support was provided by the French Federation for Magnetic Fusion Studies (FR-FCM) and the Eurofusion Consortium, funded by the Euratom Research and Training Programme (Grant Agreement No. 633053). The views and opinions expressed herein do not necessarily reflect those of the European Commission. Support was provided by the Agence Nationale de la Recherche (ANR), project CM2E (ANR-20-CE46-0010-01). The authors acknowledge the Grand Équipement National de Calcul Intensif (GENCI) for granting access to the HPC resources of IDRIS (Allocation No. AD012A01664R1) and thank the Centre de Calcul Intensif d’Aix-Marseille for its computing resources. Z.L. thanks KU Leuven for its hospitality. The work of J-C.N. was partially supported by the NSERC Discovery Grant program.

References

- [1] F. ALLMANN-RAHN, S. LAUTENBACH, M. DEISENHOFER, AND R. GRAUER, *The muphyii code: Multiphysics plasma simulation on large HPC systems*, Comput. Phys. Commun., 296 (2024), p. 109064, <https://doi.org/10.1016/j.cpc.2023.109064>.
- [2] T. D. ARBER AND R. G. L. VANN, *A Critical Comparison of Eulerian-Grid-Based Vlasov Solvers*, J. Comput. Phys., 180 (2002), pp. 339–357, <https://doi.org/10.1006/jcph.2002.7098>.
- [3] T. ARSHAD, Y. CHEN, AND G. TÓTH, *Adaptive mesh refinement in semi-implicit particle-in-cell method*, Comput. Phys. Commun., 316 (2025), p. 109806, <https://doi.org/10.1016/j.cpc.2025.109806>.
- [4] F. BACCHINI, *Relsim: A relativistic semi-implicit method for particle-in-cell simulations*, Astrophys. J. Suppl. Ser., 268 (2023), <https://doi.org/10.3847/1538-4365/acefba>.
- [5] F. BACCHINI, J. AMAYA, AND G. LAPENTA, *The relativistic implicit particle-in-cell method*, Journal of Physics: Conference Series, 1225 (2019), p. 012011, <https://doi.org/10.1088/1742-6596/1225/1/012011>.
- [6] J.-P. BÄHNER, L. PODAVINI, A. BANON NAVARRO, M. PORKOLAB, S. K. HANSEN, E. M. EDLUND, A. VON STECHOW, S. A. BOZHENKOV, O. P. FORD, G. FUCHERT, ET AL., *Magnetic geometry effects on turbulent density fluctuations in wendelstein 7-x*, Nucl. Fusion.
- [7] C. K. BIRDSALL AND A. B. LANGDON, *Plasma physics via computer simulation*, CRC press, 2018.
- [8] E. BOURNE, V. GRANDGIRARD, Y. ASAHI, J. BIGOT, P. DONNEL, A. HOFFMANN, A. KARA, P. KRAH, B. LEGOUIX, E. MALABOEUF, ET AL., *Gyselalib++: A portable c++ library for semi-lagrangian kinetic and gyrokinetic simulations*, J. Open Source Softw., 10 (2025), p. 8582.
- [9] E. BOURNE, Y. MUNSCHY, V. GRANDGIRARD, M. MEHRENBERGER, AND P. GHENDRIH, *Non-uniform splines for semi-Lagrangian kinetic simulations of the plasma sheath*, J. Comput. Phys., 488 (2023), p. 112229, <https://doi.org/https://doi.org/10.1016/j.jcp.2023.112229>, <https://www.sciencedirect.com/science/article/pii/S0021999123003248>.
- [10] J. BRACKBILL AND D. FORSLUND, *An implicit method for electromagnetic plasma simulation in two dimensions*, J. Comput. Phys., 46 (1982), pp. 271–308, [https://doi.org/10.1016/0021-9991\(82\)90016-X](https://doi.org/10.1016/0021-9991(82)90016-X).
- [11] H. BURAU, R. WIDERA, W. HÖNIG, G. JUCKELAND, A. DEBUS, T. KLUGE, U. SCHRAMM, T. E. COWAN, R. SAUERBREY, AND M. BUSSMANN, *Picongpu: A fully relativistic particle-in-cell code for a GPU cluster*, IEEE Trans. Plasma Sci., 38 (2010), pp. 2831–2839, <https://doi.org/10.1109/TPS.2010.2064310>.
- [12] C.-Z. CHENG AND G. KNORR, *The integration of the Vlasov equation in configuration space*, J. Comput. Phys., 22 (1976), pp. 330–351.
- [13] G.-H. COTTET, *Semi-Lagrangian particle methods for high-dimensional Vlasov–Poisson systems*, J. Comput. Phys., 365 (2018), pp. 362–375, <https://doi.org/10.1016/j.jcp.2018.03.042>.
- [14] G.-H. COTTET, J.-M. ETANCELIN, F. PERIGNON, AND C. PICARD, *High order semi-Lagrangian particle methods for transport equations: numerical analysis and implementation issues*, ESAIM Math. Model. Numer. Anal., 48 (2014), p. 1029–1060, <https://doi.org/10.1051/m2an/2014009>.

[15] G.-H. COTTET AND P.-A. RAVIART, *Particle methods for the one-dimensional Vlasov–Poisson equations*, SIAM J. Numer. Anal., 21 (1984), pp. 52–76, <https://doi.org/10.1137/0721003>.

[16] G. H. COTTET AND P. A. RAVIART, *On particle-in-cell methods for the Vlasov–Poisson equations*, Transport Theory Stat. Phys., 15 (1986), pp. 1–31, <https://doi.org/10.1080/00411458608210442>.

[17] N. CROUSEILLES, M. MEHRENBERGER, AND F. VECIL, *Discontinuous Galerkin semi-Lagrangian method for Vlasov–Poisson*, in ESAIM: Proceedings, vol. 32, EDP Sciences, 2011, pp. 211–230.

[18] N. CROUSEILLES, T. RESPAUD, AND E. SONNENDRÜCKER, *A forward semi-Lagrangian method for the numerical solution of the Vlasov equation*, Comput. Phys. Commun., 180 (2009), pp. 1730–1745.

[19] J. DEROUILLAT, A. BECK, F. PÉREZ, T. VINCI, M. CHIARAMELLO, A. GRASSI, M. FLÉ, G. BOUCHARD, I. PLOTNIKOV, N. AUNAI, J. DARGENT, C. RICONDA, AND M. GRECH, *Smilei : A collaborative, open-source, multi-purpose particle-in-cell code for plasma simulation*, Comput. Phys. Commun., 222 (2018), pp. 351–373, <https://doi.org/10.1016/j.cpc.2017.09.024>.

[20] L. EINKEMMER, *High performance computing aspects of a dimension independent semi-Lagrangian discontinuous Galerkin code*, Comput. Phys. Commun., 202 (2016), pp. 326–336.

[21] L. EINKEMMER, *A performance comparison of semi-Lagrangian discontinuous Galerkin and spline based Vlasov solvers in four dimensions*, J. Comput. Phys., 376 (2019), pp. 937–951, <https://doi.org/10.1016/j.jcp.2018.10.012>.

[22] L. EINKEMMER AND A. MORIGGL, *Semi-Lagrangian 4d, 5d, and 6d kinetic plasma simulation on large-scale GPU-equipped supercomputers*, Int. J. High Perform. Comput. Appl., 37 (2023), pp. 180–196, <https://doi.org/10.1177/10943420221137599>.

[23] M. EVANS AND F. HARLOW, *The particle-in-cell method for hydrodynamic calculations*, Report LA-2139, Los Alamos Scientific laboratory of the university of California, (1957).

[24] S. FASOULAS, C.-D. MUNZ, M. PFEIFFER, J. BEYER, T. BINDER, S. COPPLESTONE, A. MIRZA, P. NIZENKOV, P. ORTWEIN, AND W. RESCHKE, *Combining particle-in-cell and direct simulation Monte Carlo for the simulation of reactive plasma flows*, Phys. Fluids, 31 (2019), p. 072006, <https://doi.org/10.1063/1.5097638>.

[25] L. FEDELI, A. HUEBL, F. BOILLOD-CERNEUX, T. CLARK, K. GOTTL, C. HILLAIRET, S. JAURE, A. LEBLANC, R. LEHE, A. MYERS, C. PIECHURSKI, M. SATO, N. ZAIM, W. ZHANG, J.-L. VAY, AND H. VINCENTI, *Pushing the frontier in the design of laser-based electron accelerators with groundbreaking mesh-refined particle-in-cell simulations on exascale-class supercomputers*, in SC22: International Conference for High Performance Computing, Networking, Storage and Analysis, 2022, pp. 1–12, <https://doi.org/10.1109/SC41404.2022.00008>.

[26] E. FIJALKOW, *A numerical solution to the Vlasov equation*, Comput. Phys. Commun., 116 (1999), pp. 319–328, [https://doi.org/10.1016/S0010-4655\(98\)00146-5](https://doi.org/10.1016/S0010-4655(98)00146-5).

[27] F. FILBET AND E. SONNENDRÜCKER, *Numerical methods for the Vlasov equation*, in Numer. Math. Adv. Appl., Milano, 2003, Springer Milan, pp. 459–468.

[28] F. FILBET, E. SONNENDRÜCKER, AND P. BERTRAND, *Conservative numerical schemes for the Vlasov equation*, J. Comput. Phys., 172 (2001), pp. 166–187, <https://doi.org/10.1006/jcph.2001.6818>.

[29] V. GRANDGIRARD, J. ABITEBOUL, J. BIGOT, T. CARTIER-MICHAUD, N. CROUSEILLES, G. DIF-PRADALIER, C. EHRLACHER, D. ESTEVE, X. GARRET, P. GHENDRIH, G. LATU,

M. MEHRENBERGER, C. NORSCINI, C. PASSERON, F. ROZAR, Y. SARAZIN, E. SONNENDRÜCKER, A. STRUGAREK, AND D. ZARZOSO, *A 5d gyrokinetic full-f global semi-lagrangian code for flux-driven ion turbulence simulations*, Comput. Phys. Commun., 207 (2016), pp. 35–68, <https://doi.org/https://doi.org/10.1016/j.cpc.2016.05.007>, <https://www.sciencedirect.com/science/article/pii/S0010465516301230>.

- [30] T. GÖRLER, X. LAPILLONNE, S. BRUNNER, T. DANNERT, F. JENKO, F. MERZ, AND D. TOLD, *The global version of the gyrokinetic turbulence code GENE*, J. Comput. Phys., 230 (2011), pp. 7053–7071, <https://doi.org/https://doi.org/10.1016/j.jcp.2011.05.034>.
- [31] R. HATZKY, A. KÖNIES, AND A. MISHCHENKO, *Electromagnetic gyrokinetic pic simulation with an adjustable control variates method*, J. Comput. Phys., 225 (2007), pp. 568–590, <https://doi.org/10.1016/j.jcp.2006.12.019>.
- [32] R. HATZKY, T. M. TRAN, A. KÖNIES, R. KLEIBER, AND S. J. ALLFREY, *Energy conservation in a nonlinear gyrokinetic particle-in-cell code for ion-temperature-gradient-driven modes in θ -pinch geometry*, Phys. Plasmas, 9 (2002), pp. 898–912, <https://doi.org/10.1063/1.1449889>.
- [33] R. W. HOCKNEY AND J. W. EASTWOOD, *Computer simulation using particles*, CRC Press, 2021.
- [34] F. JENKO, W. DORLAND, M. KOTSCHENREUTHER, AND B. ROGERS, *Electron temperature gradient driven turbulence*, Phys. Plasmas, 7 (2000), pp. 1904–1910.
- [35] F. JENKO, W. DORLAND, M. KOTSCHENREUTHER, AND B. N. ROGERS, *Electron temperature gradient driven turbulence*, Phys. Plasmas, 7 (2000), pp. 1904–1910, <https://doi.org/10.1063/1.874014>.
- [36] F. JENKO AND THE GENE DEVELOPMENT TEAM, *The GENE code*. <https://genecode.org/>, March 2011. Accessed: January 30, 2026.
- [37] J. JUNO, A. HAKIM, J. TENBARGE, E. SHI, AND W. DORLAND, *Discontinuous Galerkin algorithms for fully kinetic plasmas*, J. Comput. Phys., 353 (2018), pp. 110–147, <https://doi.org/10.1016/j.jcp.2017.10.009>.
- [38] M. KIRCHHART AND R. P. WILHELM, *The numerical flow iteration for the Vlasov–Poisson equation*, SIAM J. Sci. Comput., 46 (2024), pp. A1972–A1997.
- [39] R. KLEIBER, M. BORCHARDT, R. HATZKY, A. KÖNIES, H. LEYH, A. MISHCHENKO, J. RIEMANN, C. SLABY, J. GARCÍA-REGAÑA, E. SÁNCHEZ, AND M. COLE, *Euterpe: A global gyrokinetic code for stellarator geometry*, Comput. Phys. Commun., 295 (2024), p. 109013, <https://doi.org/https://doi.org/10.1016/j.cpc.2023.109013>, <https://www.sciencedirect.com/science/article/pii/S0010465523003582>.
- [40] K. KORMANN, K. REUTER, AND M. RAMPP, *A massively parallel semi-Lagrangian solver for the six-dimensional Vlasov–Poisson equation*, Int. J. High Perform. Comput. Appl., 33 (2019), pp. 924–947, <https://doi.org/10.1177/1094342019834644>.
- [41] K. KORMANN AND E. SONNENDRÜCKER, *Sparse grids for the Vlasov–Poisson equation*, in Sparse Grids and Applications - Stuttgart 2014, J. Gärcke and D. Pflüger, eds., Cham, 2016, Springer International Publishing, pp. 163–190.
- [42] P. KRAH, X.-Y. YIN, J. BERGMANN, J.-C. NAVÉ, AND K. SCHNEIDER, *A characteristic mapping method for Vlasov–Poisson with extreme resolution properties*, Commun. Comput. Phys., 35 (2024), p. 905–937, <https://doi.org/10.4208/cicp.oa-2024-0012>, <http://dx.doi.org/10.4208/cicp.0A-2024-0012>.

[43] M. KRAUS, K. KORMANN, P. J. MORRISON, AND E. SONNENDRÜCKER, *GEMPIC: geometric electromagnetic particle-in-cell methods*, J. Plasma Phys., 83 (2017), p. 905830401, <https://doi.org/10.1017/S002237781700040X>.

[44] G. LAPENTA, *Exactly energy conserving semi-implicit particle in cell formulation*, J. Comput. Phys., 334 (2017), pp. 349–366, <https://doi.org/10.1016/j.jcp.2017.01.002>.

[45] G. LAPENTA, J. BRACKBILL, AND P. RICCI, *Kinetic approach to microscopic-macroscopic coupling in space and laboratory plasmas*, Phys. Plasmas, 13 (2006), <https://doi.org/10.1063/1.2173623>.

[46] G. LAPENTA, D. SCHRIVER, R. J. WALKER, J. BERCHEM, N. F. ECHTERLING, M. EL ALAOUI, AND P. TRAVNICEK, *Do we need to consider electrons' kinetic effects to properly model a planetary magnetosphere: The case of mercury*, J. Geophys. Res.: Space Phys., 127 (2022), p. e2021JA030241, <https://doi.org/10.1029/2021JA030241> e2021JA030241 2021JA030241.

[47] J. LION, J.-C. ANGLÈS, L. BONAUER, A. B. NAVARRO, S. C. CERON, R. DAVIES, M. DREVLAK, N. FOPPIANI, J. GEIGER, A. GOODMAN, ET AL., *Stellaris: A high-field quasi-isodynamic stellarator for a prototypical fusion power plant*, Fusion Eng. Des., 214 (2025), p. 114868.

[48] N. R. MANDELL, A. HAKIM, G. W. HAMMETT, AND M. FRANCISQUEZ, *Electromagnetic full-f gyrokinetics in the tokamak edge with discontinuous Galerkin methods*, J. Plasma Phys., 86 (2020), p. 905860109, <https://doi.org/10.1017/S0022377820000070>.

[49] S. MARKIDIS, G. LAPENTA, AND RIZWAN-UDDIN, *Multi-scale simulations of plasma with iPIC3D*, Math. Comput. Simul., 80 (2010), pp. 1509–1519, <https://doi.org/10.1016/j.matcom.2009.08.038>. Multiscale modeling of moving interfaces in materials.

[50] R. J. MASON, *Implicit moment particle simulation of plasmas*, J. Comput. Phys., 41 (1981), pp. 233–244, [https://doi.org/10.1016/0021-9991\(81\)90094-2](https://doi.org/10.1016/0021-9991(81)90094-2).

[51] O. MERCIER, X.-Y. YIN, AND J.-C. NAVE, *The characteristic mapping method for the linear advection of arbitrary sets*, SIAM J. Sci. Comput., 42 (2020), pp. A1663–A1685, <https://doi.org/10.1137/18M1234424>, <https://doi.org/10.1137/18M1234424>, <https://arxiv.org/abs/https://doi.org/10.1137/18M1234424>.

[52] A. MYERS, P. COLELLA, AND B. STRAALEN, *A 4th-order particle-in-cell method with phase-space remapping for the Vlasov–Poisson equation*, SIAM J. Sci. Comput., 39 (2016), pp. B467–B485, <https://doi.org/10.1137/16M105962X>.

[53] J.-C. NAVE, R. R. ROSALES, AND B. SEIBOLD, *A gradient-augmented level set method with an optimally local, coherent advection scheme*, J. Comput. Phys., 229 (2010), pp. 3802–3827, <https://doi.org/https://doi.org/10.1016/j.jcp.2010.01.029>, <https://www.sciencedirect.com/science/article/pii/S0021999110000525>.

[54] M. PALMROTH, U. GANSE, Y. PFAU-KEMPF, M. BATTARBEE, L. TURC, T. BRITO, M. GRANDIN, S. HOILIJOKI, A. SANDROOS, AND S. VON ALFTAN, *Vlasov methods in space physics and astrophysics*, Living Rev. Comput. Astrophys., 4 (2018), p. 1.

[55] M. PALMROTH, U. GANSE, Y. PFAU-KEMPF, M. BATTARBEE, L. TURC, T. BRITO, M. GRANDIN, S. HOILIJOKI, A. SANDROOS, AND S. VON ALFTAN, *Vlasov methods in space physics and astrophysics*, Living Rev. Comput. Astrophys., 4 (2018), p. 1, <https://doi.org/10.1007/s41115-018-0003-2>.

[56] P. PARODI, S. BOCCELLI, F. BARISELLI, AND T. MAGIN, *Pantera: A PIC-MCC-DSMC software for the simulation of rarefied gases and plasmas*, SoftwareX, 31 (2025), p. 102244, <https://doi.org/10.1016/j.softx.2025.102244>.

[57] L. P. RIISHØJGAARD, S. E. COHN, Y. LI, AND R. MÉNARD, *The use of spline interpolation in semi-Lagrangian transport models*, Monthly Weather Review, 126 (1998), pp. 2008 – 2016, [https://doi.org/10.1175/1520-0493\(1998\)126<2008: TUOSII>2.0.CO;2](https://doi.org/10.1175/1520-0493(1998)126<2008: TUOSII>2.0.CO;2).

[58] J. A. ROSSMANITH AND D. C. SEAL, *A positivity-preserving high-order semi-Lagrangian discontinuous Galerkin scheme for the Vlasov–Poisson equations*, J. Comput. Phys., 230 (2011), pp. 6203–6232, <https://doi.org/10.1016/j.jcp.2011.04.018>.

[59] H. SCHMITZ AND R. GRAUER, *Kinetic Vlasov simulations of collisionless magnetic reconnection*, Phys. Plasmas, 13 (2006), p. 092309, <https://doi.org/10.1063/1.2347101>.

[60] E. SONNENDRÜCKER, J. ROCHE, P. BERTRAND, AND A. GHIZZO, *The semi-Lagrangian method for the numerical resolution of the Vlasov equation*, J. Comput. Phys., 149 (1999), pp. 201–220.

[61] S. TAYLOR AND J.-C. NAVÉ, *A characteristic mapping method for incompressible hydrodynamics on a rotating sphere*, arXiv preprint arXiv:2302.01205, (2023).

[62] D. VERSCHAREN, K. KLEIN, AND B. MARUCA, *The multi-scale nature of the solar wind*, Living Rev. Sol. Phys., 16 (2019), <https://doi.org/10.1007/s41116-019-0021-0>.

[63] D. VERSCHAREN, R. T. WICKS, O. ALEXANDROVA, R. BRUNO, D. BURGESS, C. H. CHEN, R. D’AMICIS, J. DE KEYSER, T. D. DE WIT, L. FRANCI, ET AL., *A case for electron-astrophysics*, Experimental Astronomy, 54 (2022), pp. 473–519.

[64] P. VIDAL, E. BOURNE, V. GRANDGIRARD, M. MEHRENBERGER, AND E. SONNENDRÜCKER, *Local cubic spline interpolation for vlasov-type equations on a multi-patch geometry*, arXiv preprint arXiv:2505.22078, (2025).

[65] B. WANG, S. ETHEIER, W. TANG, T. WILLIAMS, K. Z. IBRAHIM, K. MADDURI, S. WILLIAMS, AND L. OLICKER, *Kinetic turbulence simulations at extreme scale on leadership-class systems*, in Proceedings of the International Conference on High Performance Computing, Networking, Storage and Analysis, SC ’13, New York, NY, USA, 2013, Association for Computing Machinery, <https://doi.org/10.1145/2503210.2503258>, <https://doi.org/10.1145/2503210.2503258>.

[66] B. WANG, G. H. MILLER, AND P. COLELLA, *A particle-in-cell method with adaptive phase-space remapping for kinetic plasmas*, SIAM J. Sci. Comput., 33 (2011), pp. 3509–3537, <https://doi.org/10.1137/100811805>.

[67] R.-P. WILHELM, J. EIFERT, M. TORRILHON, AND F. ORLAND, *High fidelity simulations of the multi-species Vlasov equation in the electro-static, collisional-less limit*, Plasma Phys. Controlled Fusion, 67 (2025), p. 025011, <https://doi.org/10.1088/1361-6587/ad9fdb>.

[68] R. P. WILHELM AND M. KIRCHHART, *An interpolating particle method for the Vlasov–Poisson equation*, J. Comput. Phys., 473 (2023), p. 111720, <https://doi.org/10.1016/j.jcp.2022.111720>.

[69] R.-P. WILHELM, M. KIRCHHART, AND M. TORRILHON, *Introduction to the numerical flow iteration for the Vlasov–Poisson equation*, PAMM, 23 (2023), p. e202300162, <https://doi.org/10.1002/pamm.202300162>.

[70] R.-P. WILHELM AND K. KORMANN, *Restarting the numerical flow iteration through low rank tensor approximations*, arXiv preprint arXiv:2509.08474, (2025).

[71] B. YADAV, *Characteristic mapping method for incompressible Euler equations*, master’s thesis, McGill University, Montréal, Canada, 2015. Available at https://raw.githubusercontent.com/CharacteristicMappingMethod/characteristicmappingmethod.github.io/main/assets/thesis/badal_yadav_master.pdf.

- [72] X.-Y. YIN, P. KRAH, J.-C. NAVE, AND K. SCHNEIDER, *A characteristic mapping method with source terms: Applications to ideal magnetohydrodynamics*, arXiv preprint arXiv:2411.13772, (2024).
- [73] X.-Y. YIN, O. MERCIER, B. YADAV, K. SCHNEIDER, AND J.-C. NAVE, *A Characteristic Mapping Method for the Two-Dimensional Incompressible Euler Equations*, J. Comput. Phys., 424 (2021), p. 109781, <https://doi.org/10.1016/j.jcp.2020.109781>.
- [74] X.-Y. YIN, K. SCHNEIDER, AND J.-C. NAVE, *A characteristic mapping method for the three-dimensional incompressible Euler equations*, J. Comput. Phys., 477 (2023), p. 111876.